



Integrating CdS quantum dots on hollow graphitic carbon nitride nanospheres for hydrogen evolution photocatalysis

Dandan Zheng, Guigang Zhang, Xinchen Wang*

State Key Laboratory of Photocatalysis on Energy and Environment, College of Chemistry, Fuzhou University, Fuzhou 350002, PR China



ARTICLE INFO

Article history:

Received 16 April 2015

Received in revised form 26 May 2015

Accepted 29 May 2015

Available online 1 June 2015

Keywords:

Conjugated polymer

Photocatalysis

Heterojunction

Hollow nanospheres

Quantum dots

ABSTRACT

Inorganic quantum dots (QDs) have been introduced onto the exterior surface of hollow carbon nitride spheres (HCNS) to construct an inorganic-polymeric curved heterostructure for solar energy conversion. This hybrid nanoheterostructure cooperates well with cofactors to achieve efficient hydrogen evolution under visible light illumination. The enhanced photocatalytic performance of the heterostructure can be attributed to the unique three-dimensional (3D) hollow architectural framework of HCNS as a polymeric scaffold to form intimate interfacial contact with the QDs by a self-assembly strategy to facilitate surface kinetics of charge separation and mass transfer. Such inorganic-polymer hybrid nanoarchitectures based on controlled deposition of stiff QDs onto the flexible HCNS surface provide a valuable platform for constructing stable photoredox systems for solar-to-chemical conversion. This result promises the great potentials of biostructurally-mimic hollow soft semiconductors in developing photofunctional architectures, with an ample choice of secondary guest species to selectively engineer the interface physicochemistry of the hollow sphere for solar application.

© 2015 Elsevier B.V. All rights reserved.

1. Introduction

Solar energy conversion has been suggested as a renewable and sustainable alternative energy resource to fossil reserves [1–2]. Photocatalytic water splitting by a semiconductor is one of the attractive candidates for clean energy production. During the past 40 years, the search for highly-efficient semiconductor photocatalysts with narrow band gap energy and suitable redox potentials has been actively investigated to develop artificial photosynthetic systems for water splitting via sunlight [3–5].

Similar to widely-studied wide band-gap semiconductors such as metal oxides, metal chalcogenides have also been intensively investigated due to their inherent feature of narrow band-gap [6–7]. Specifically, CdS has a conduction band (CB) edge sufficiently more negative than the reduction potential of proton and it has a relatively narrow band gap of 2.2 eV, which can absorb sunlight with wavelength <560 nm to catalyze water reduction half-reaction to release H₂ gas [8]. Thus, CdS could potentially act as functional building units of water reduction to cooperate with water photooxidation couplers to establish full water splitting to literate O₂ and H₂ by a two-photon excitation fashion, similar to the biological Z-scheme system, where photofunctional motifs and cofactors

are integrated on the surface of permeable hollow thylakoid membrane [9–11]. This motivates much investigation in metal chalcogenides and their modifications for solar water splitting, while still biomimetically-developing photosynthetically-relevant soft hollow nanostructures with self-healing functions to mediate charge and energy transfer [12–15]. However, the reduced band gap energy makes chalcogenides much less stable than most wide band-gap semiconductors, especially when surface charge buildup occurs without kinetic controls on the migration and transfer of charge carriers. In the most studied system, that of the CdS based catalysts, the photocorrosion problem is still a concern in that the sulfide ion is prone to oxidation by light-triggered holes [16]. Thus, kinetic controls in the reaction selectivity of the holes are crucial in metal chalcogenide photocatalysis.

Some methods have been emerged to inhibit the photocorrosion of CdS. One approach is to form CdS core/shell nanostructures using carbon films and polymers to chemically protect the inner CdS nanoparticles [17–18]. Another approach is the coupling of CdS with secondary semiconductors (TiO₂, ZnO, CdSe, etc.) to form heterojunctions to release charge buildup by accelerating charge transfer and migration [19–20]. Gao et al. incorporated a spherical CdTe core covered by a rod-shaped CdS shell to produce a new class of heterojunction system, and such hetero-nanostructures can exhibit a high performance [21]. The combination of two semiconductors enables semiconductor band alignments to promote charge separation. Namely, the photoinduced holes can directly

* Corresponding author. Tel.: +86 591 83920097; fax: +86 591 83920097.

E-mail address: xcwang@fzu.edu.cn (X. Wang).

and quickly transfer from CdS to the combined semiconductor and thus alleviate the damage to CdS. Additional loading of oxidative co-catalysts on CdS as hole trappers, such as RuO₂ and IrO₂, can further protect it from being oxidized, while stabilizing the light-triggered electron for the reduction reaction. Such a heterojunction design provides a useful tool to create novel composite materials and devices for artificial photosynthesis.

Recently, melon-based graphitic carbon nitride (termed here as g-C₃N₄ for simplicity) has emerged as a new family of polymer photocatalysts due to its unique physicochemical properties [22–24]. Thus, far, CdS/g-C₃N₄ hybrids have been investigated [25–28]. The CB offset between g-C₃N₄ and CdS can drive the migration of electrons from g-C₃N₄ to CdS, while holes are transferred from CdS to g-C₃N₄ by the valence band (CV) offset, thus locally separating electrons and holes as well as isolating the later reduction and oxidation reactions in nanospace. The previous papers overwhelmingly focus on conventional g-C₃N₄ with un-optimized texture that suffers from sluggish reaction and charge-separation kinetics, as well as low light harvesting capability [26]. To make the system photochemically more efficient, the texturization of the conjugated semiconductor in the form of stable hollow nanostructure with controlled size, dimension, shell thickness and surface functionalities is certainly desired, which however challenges materials chemists and designers since most hollow polymer nanospheres are typically subjected to deformation.

Here, we describe HCNS as robust polymeric scaffolds to integrate and stabilize inorganic semiconductor QDs. Crucial to the physical properties of these free-standing hollow nanosphere polymer is their extreme morphological, thermal and chemical stability against sintering in the air up to 500 °C [29]. This stable hollow conjugated structure could allow for designing functional nanoarchitectures, with large and interconnected exterior and interior surfaces that increase the amount of light absorbed and promote surface-dependent reactions by shuttling both the electronic and chemical species via the porous shell. The resulting 3D architectures of HCNS can not only provide large, accessible interface to host QDs for fast charge separation, but are also conducive to transporting reactants to the active sites. In addition, the embedding of inorganic nanoparticles in the nitrogen-rich polymeric framework is an effective approach to solve their aggregation problem during operation conditions. For all these reasons, we are interested in combining inorganic QDs (i.e., CdS, CdSe, MoS₂) and even Au-modified QDs (data no shown here) with HCNS to construct complex photoredox systems for H₂ production, and herein as exemplified by CdS-HCNS hybrids.

In brief, HCNS was synthesized using silica templates according to our earlier paper [30–31]. CdS QDs were then introduced onto the exterior surface of HCNS by a interface self-assembly method [32–34]. The resultant heterojunctions allow for the absorption of light in the bulk semiconductor domains to form excitons, followed by effective charge generation and separation at the material interfaces. The samples were named as xCdS-HCNS, where x (1–4) is corresponded to weight percentages of CdS QDs for 10, 20, 30, and 40 wt.%, respectively, according to HCNS weight. The morphology, structure and optical/electric properties of the samples were characterized with various physicochemical techniques, while the performance of these samples was accessed in a H₂ production assay.

2. Experimental

2.1. Synthesis of photocatalysts

Synthesis of HCNS: HCNS was prepared by thermal polymerization according to the literature [30]. First, the monodisperse

SiO₂ template were synthesized according to the Stöber method. Briefly, 3.10 g of aqueous ammonia (32 wt.%, Sigma–Aldrich) and 10 g of deionised water were added in 58.5 g of ethanol to from a mixture solution after stirring for 30 min at 30 °C. 5.6 mL of tetraethoxysilane (TEOS, Sigma–Aldrich) was added to the above solution with vigorous stirring and was left stationary for 1 h to yield uniform nonporous silica spheres. A mixture of adequate TEOS and n-octadecyltrimethoxysilane (C₁₈TMOS, Sigma–Aldrich) was then added dropwise to the above solution with magnetic stirring, sat quietly maturing for another 3 h at ambient temperature. The nanostructured silica was centrifuged, dried at 70 °C and calcined at 550 °C for 6 h in air. The as-prepared monodisperse SiO₂ templates were neutralized with a 1-M HCl solution and then dried at 80 °C overnight. Then, these monodisperse silica nanoparticles were used as a template to prepare HCNS. 2 g of the SiO₂ template was added to 10 g of cyanamide (Alfa Aesar), and kept under sonication and vacuum at 60 °C for 2 h. After that, the mixture was stirred at 60 °C overnight, which was then centrifuged, dried, and calcined at 550 °C for 4 h. The obtained powder was treated with 4 M NH₄HF₂ for 12 h to remove the silica template, then centrifuged and washed three times with distilled water and once with ethanol. The final yellow HCNS powders were obtained by drying at 80 °C in a vacuum oven overnight.

Synthesis of xCdS-HCNS: A suitable amount of Cd(Ac)₂ (Cd(CH₃COO)₂·2H₂O Alfa Aesar, 99%) was dissolved in 40 mL of deionized water to form a clear solution after stirring for 30 min at room temperature. Subsequently, 20 mg prepared HCNS added in the above solution and intensely stirred over night. Then, the precipitate was harvested by centrifugation and washed several times with deionized water before being dried in oven at 60 °C for 6 h. After that, the powder was placed in a glass bottle to calcine in a furnace at 300 °C for 2 h under flowing H₂S gas. Finally, CdS-HCNS samples were obtained, denoted as xCdS-HCNS, where x (1–4) refers to the weight percentages of CdS QDs of 10, 20, 30, and 40 wt.%, according to HCNS weight.

Synthesis of HCNS-H₂S: the same method and experimental conditions with Synthesis of xCdS-HCNS, only without added Cd(Ac)₂.

Synthesis of 2CdS-SiO₂: the contrast CdS was prepared by coating 20 wt.% CdS QDs at SiO₂ spheres, which has same diameter of HCNS.

2.2. Characterization

The morphology of the sample was investigated by field emission scanning electron microscopy (SEM) (JSM-6700F). Transmission electron microscopy (TEM) was obtained by Zeis 912 microscope. The nitrogen adsorption–desorption isotherms were collected at 77 K using Micromeritics ASAP 2020 Surface Area and Porosity Analyzer. Powder X-ray diffraction (XRD) measurements were performed on Bruker D8 Advance diffractometer with Cu K α 1 radiation ($k = 1.5406 \text{ \AA}$). Fourier transformed infrared (FTIR) spectra were recorded on BioRad FTS 6000 spectrometer. X-ray photoelectron spectroscopy (XPS) data were obtained on Thermo ESCALAB250 instrument with a monochromatized Al K α line source (200 W). The solid-state ¹³C NMR spectra were collected using a Bruker Advance III 500 Spectrometer. UV–vis diffuse reflectance spectra (UV–vis DRS) were performed on Varian Cary 500 Scan UV–visible system. Photoluminescence spectra were recorded on an Edinburgh FI/FSTCSPC 920 spectrophotometer. Electron paramagnetic resonance (EPR) measurements were performed using a Bruker model A300 spectrometer. Electrochemical measurements were conducted with a BAS Epsilon Electrochemical System in a conventional three electrode cell, using a Pt plate as the counter electrode and an Ag/AgCl electrode (3 M KCl) as the reference electrode. The working electrode was prepared on indium-tin oxide (ITO) glass that was cleaned by sonication in ethanol for 30 min and dried at 353 K. The boundary of ITO glass was protected

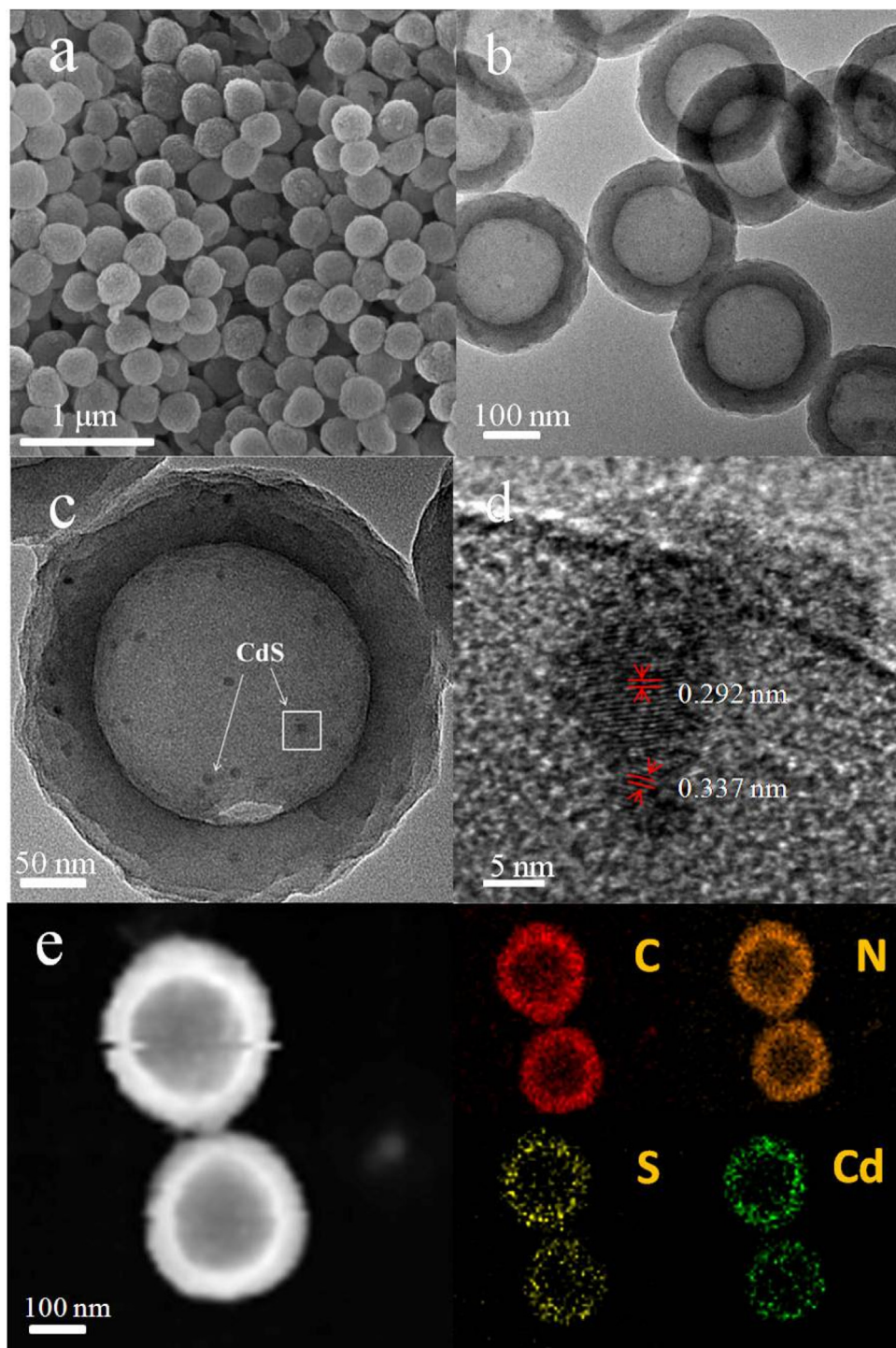


Fig. 1. Surface morphology characterization. (a) SEM, (b, c) TEM, (d) HRTEM images, and (e) elemental mapping of 2CdS-HCNS sample.

using Scotch tape. The 5 mg sample was dispersed in 1 mL of DMF by sonication to get a slurry. The slurry was spread onto pretreated ITO glass. After air-drying, the working electrode was further dried at 393 K for 2 h to improve adhesion. Then, the Scotch tape was unstuck, and the uncoated part of the electrode was isolated with epoxy resin.

2.3. Photocatalytic test

Photocatalytic H₂ production was carried out in a Pyrex top-irradiation reaction vessel connected to a glass-closed gas cir-

culation system. For each reaction, 20 mg well-ground catalyst powder was dispersed in an aqueous solution (100 mL) containing triethanolamine (10 vol.%) as sacrificial electron donor. 3 wt.% Pt was photodeposited onto the catalysts using H₂PtCl₆ dissolved in the reactant solution. The reactant solution was evacuated several times to remove air completely prior to irradiation under a 300 W Xe lamp and a water-cooling filter. The wavelength of the incident light was controlled by using an appropriate long pass cut-off filter. The temperature of the reactant solution was maintained at room temperature by a flow of cooling water during the reaction. The evolved gases were analyzed by gas chromatography equipped

with a thermal conductive detector (TCD) with argon as the carrier gas.

3. Results and discussion

The local morphologies of an optimized CdS-HCNS sample are first examined by scanning electron microscope (SEM) and transmission electron microscopy (TEM). In Fig. 1a, uniform hollow structures with a diameter of ~320 nm are retained after the post-processing, indicating the robust nature of the hollow polymer. The thus established heterostructures can be clearly observed in the TEM image because of the different electron penetrability between

Table 1
Physicochemical properties of the xCds-HCNS and HCNS samples.

Sample	C/Natomic	Cds [a][wt.%]	SA [b][m ² g ⁻¹]	PV [c][cm ³ g ⁻¹]
HCNS	0.72	0	80	0.31
HCNS-H ₂ S	0.72	0	118	0.42
1Cds-HCNS	0.72	7.2	117	0.39
2Cds-HCNS	0.73	15.7	120	0.43
3Cds-HCNS	0.73	24.9	123	0.41
4Cds-HCNS	0.73	34.1	119	0.42

[a] Calculated from elemental analysis result about S amount.

[b] BET surface area calculated from the linear part of the BET plot ($P/P_0 = 0.1\text{--}0.2$).

[c] Total pore volume, taken from the volume of N₂ adsorbed at $P/P_0 = 0.99$.

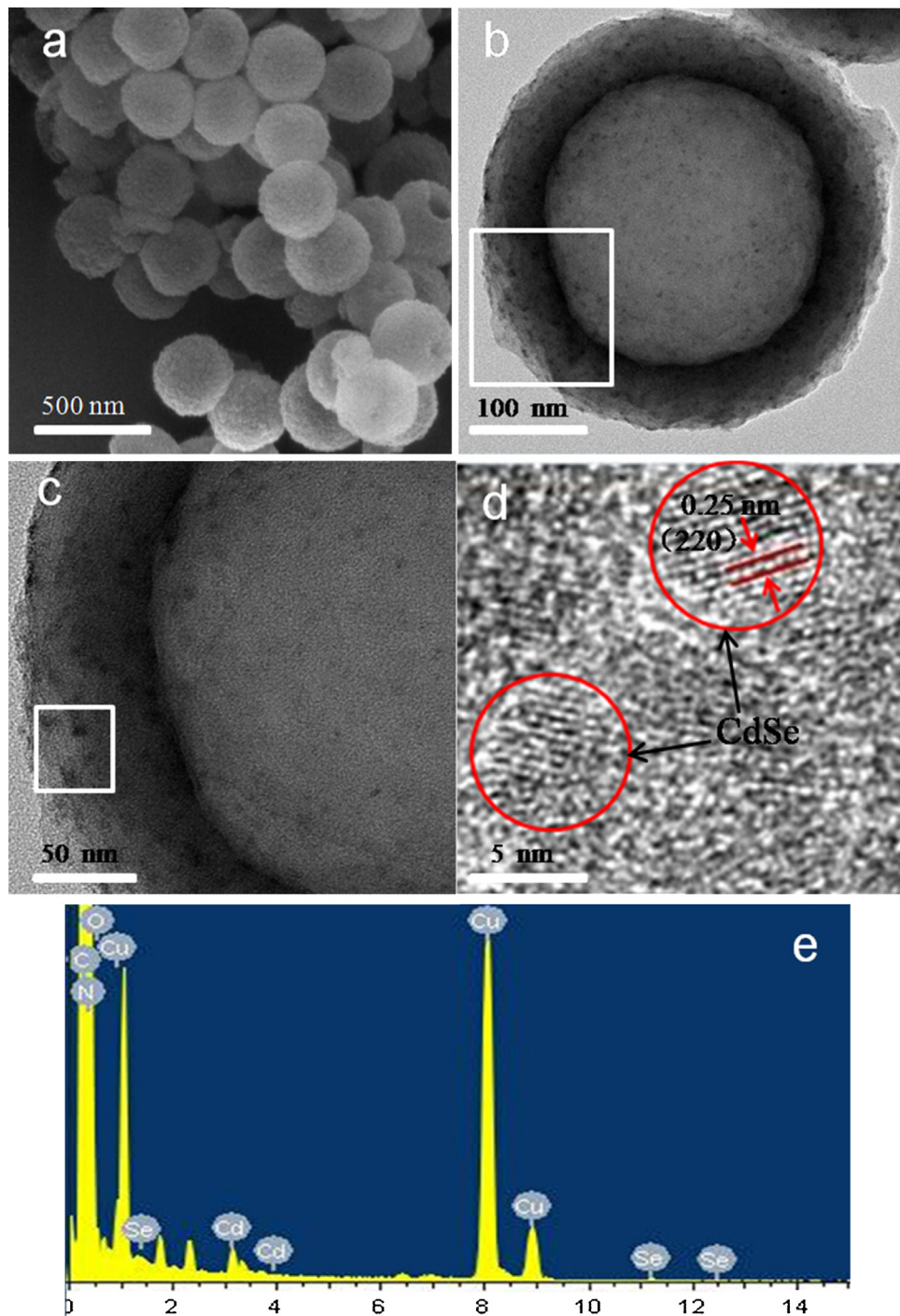


Fig. 2. (a) SEM, (b, c) TEM, and (d) HRTEM images of CdSe (JCPDS 192,191)-HCNS, (e) is the TEM-EDX spectrum of CdSe-HCNS.

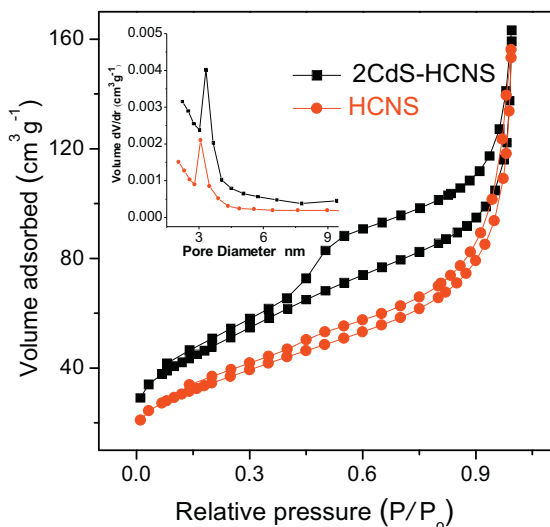


Fig. 3. N₂ adsorption-desorption isotherms and the corresponding Barrett-Joyner-Halenda pore-size distribution (inset) of 2CdS-HCNS, with HCNS as a reference.

the two phases. In Fig. 1b–c, CdS QDs of 5–7 nm in size is evenly deposited on the HCNS surface, implying that no particulate aggregation of CdS QDs occurs due to the intense stabilization effect created by the nitrogen-rich soft matrix. The HRTEM image in Fig. 1d shows one single CdS QD with clearly visible atomic lattice fringes on the surface of HCNS, suggesting a highly crystalline nature. The lattice fringes of the QDs with a *d*-spacing of 0.292 and 0.337 nm, corresponding to the inter-planar distance of the (200) and (111) planes of *fcc* CdS (JCPDS 89-0440), respectively. Fig. 1e exhibits the elemental mapping of the 2CdS-HCNS sample in dark field, further illustrating the homogeneous distribution of C, N, S, and Cd in the sphere. Moreover, as shown in Fig. 2, the SEM and TEM images present the CdSe QDs deposited on the exterior surface of HCNS to fabricate a hybrid system.

N₂-sorption analysis of the samples was investigated to study the textural parameters. In Fig. 3, a typical IV isotherm featuring with a pronounced H1-type hysteresis loop in 0.4–0.9 relative pressure (P/P₀) is observed, supporting the existence of mesopores in the polymeric frameworks. The specific surface area of the 2CdS-HCNS sample was 120 m² g⁻¹, while the pore size distributions

determined by the BJH methods show that the average pore size is ~3.6 nm. The corresponding textural parameters of xCdS-HCNS samples were shown in Table 1. Compared with pure HCNS, all modified samples exhibit relatively increased specific surface areas, while the pore volumes do not change appreciably. Similar surface area enlargement was also obtained for the reference HCNS-H₂S sample, indicating that the increased surface area is attributed to the post annealing effect [35–36].

The crystal structure of the samples was examined by powder X-ray diffraction (XRD). In Fig. 4a, the peaks centering at 13.4° and 27.4° are related to the in-plane structural repeating units of tri-*s*-triazine, and the latter one is attributed to the (002) plane with graphitic stacking of HCNS. The peaks at 46.8° and 55.5° are termed as face-centered cubic structure of typical CdS phase [37–38]. It should be noted that the broaden in the peak width at 46.8° and 55.5° are ascribed to a quantum size effect of CdS QDs [19]. The particle size of CdS QDs calculated by the Scherrer equation is ~5 nm, in good coincidence with that observed in TEM images. When increasing the loading contents of CdS QDs, no evident change can be checked in the peak position except for gradually increased peak intensities at 46.8° and 55.5°, once again confirming the good stability of the host spheres to incorporate CdS QDs.

This result was also confirmed by Fourier transform infrared (FTIR) measurements (Fig. 4b), where not any obvious change is detected for the heterostructure compared with pure HCNS. The feature-distinctive stretch modes of aromatic C=N heterocycles at 1200–1600 cm⁻¹ together with the breathing mode of the triazine units at 810 cm⁻¹, which is also very similar to that of HCNS [36]. Evidently, a reducing absorption of C=N and N=C=N groups at 2180 cm⁻¹ is observed for 2CdS-HCNS sample, indicating that the defective condensation of HCNS frameworks is greatly improved by the post thermal treatment.

X-ray photoelectron spectroscopy (XPS) measurements and elemental analysis were performed to evaluate the chemical state of 2CdS-HCNS sample. High-resolution XPS spectra of Cd 3d with two deconvoluted peaks at 411.4 eV (Cd 3d3/2) and 404.7 eV (Cd 3d5/2) are certified as Cd (II) species (Fig. 4a), whereas the peak at 162.1 eV (S 2p3/2) is ascribed to the hybrid chemical bond species of S²⁻ arising from CdS-HCNS heterostructure. The elemental analysis (Table 1) further confirms the co-existence of HCNS and CdS QDs. However, no evident difference in BE of CdS-HCNS can be viewed in comparison with HCNS (Fig. 5b, c). The carbon and nitrogen XPS analyses revealed that the HCNS has a triazine-based heterocycle,

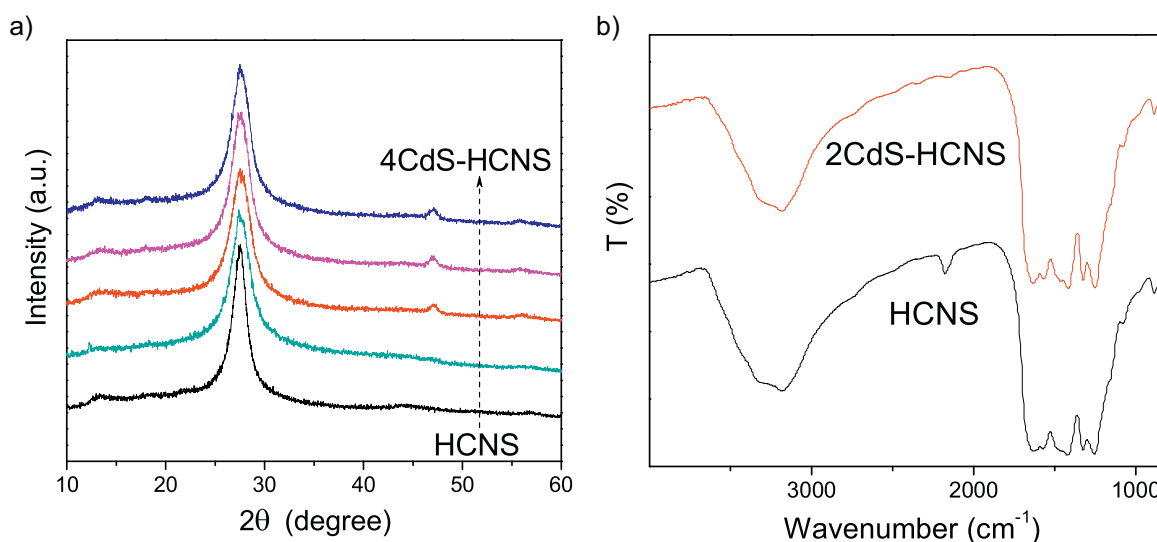


Fig. 4. (a) XRD patterns, (b) FT-IR spectra of CdS-HCNS, together with HCNS as a reference.

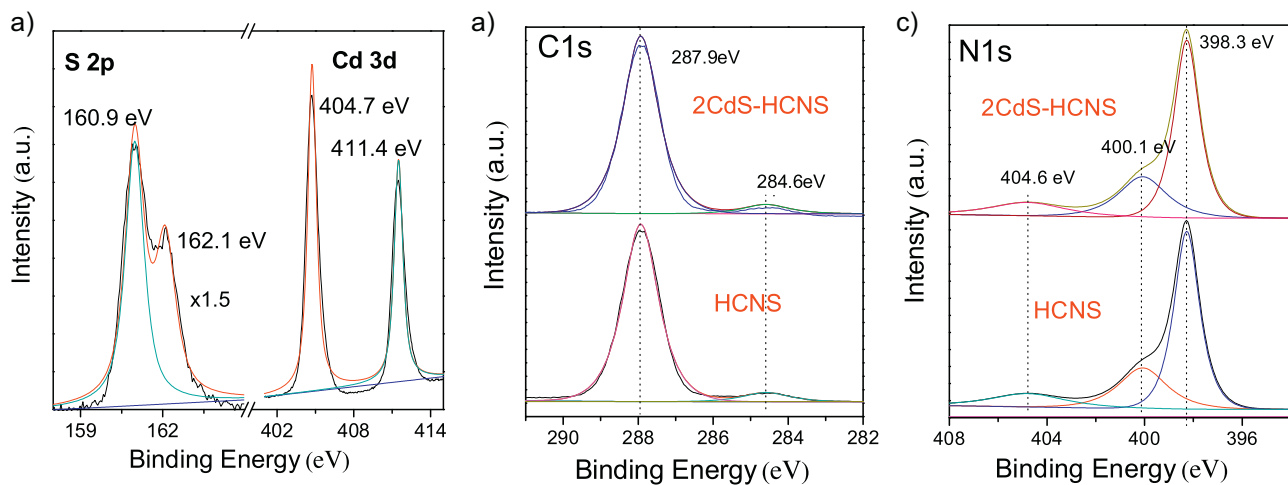


Fig. 5. XPS spectra of the 2CdS-HCNS sample. The high-resolution spectra of S2p, Cd3d (a), C1s (b) and N1s (c), with reference of HCNS.

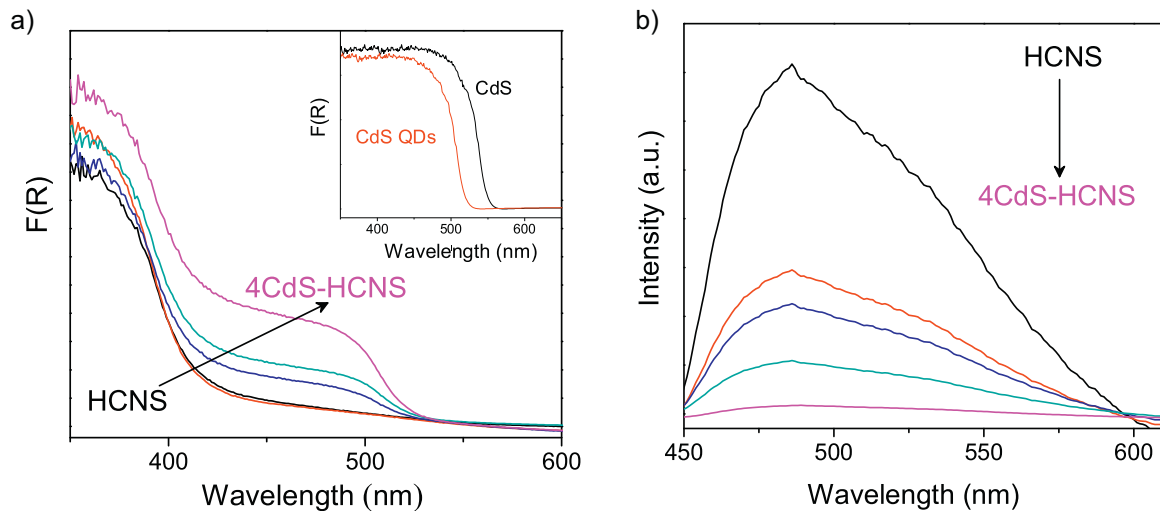


Fig. 6. (a) UV-vis diffuse reflectance spectra and (b) photoluminescence spectra of CdS-HCNS.

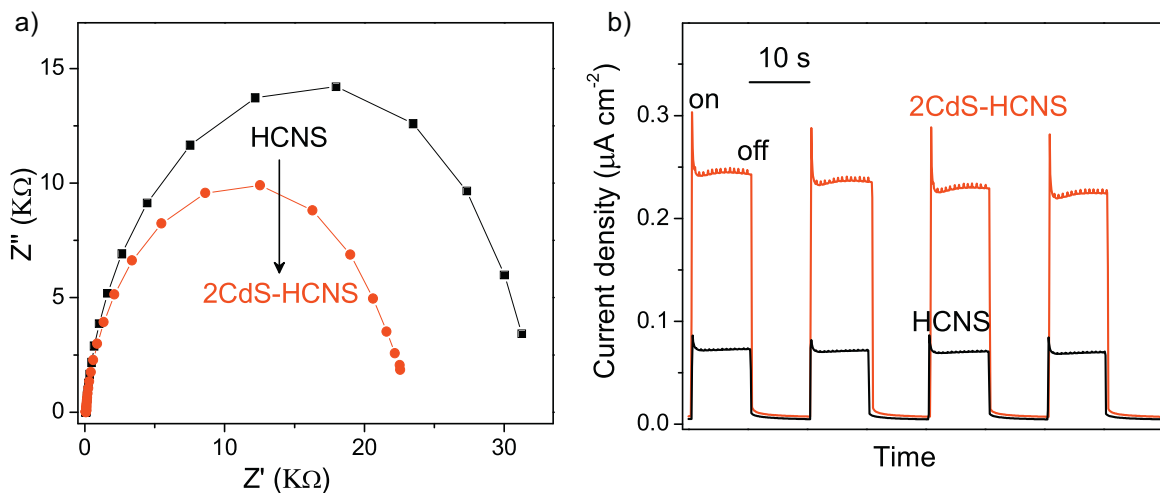


Fig. 7. (a) EIS Nyquist plots and (b) the photocurrent generation performance of CdS-HCNS electrode.

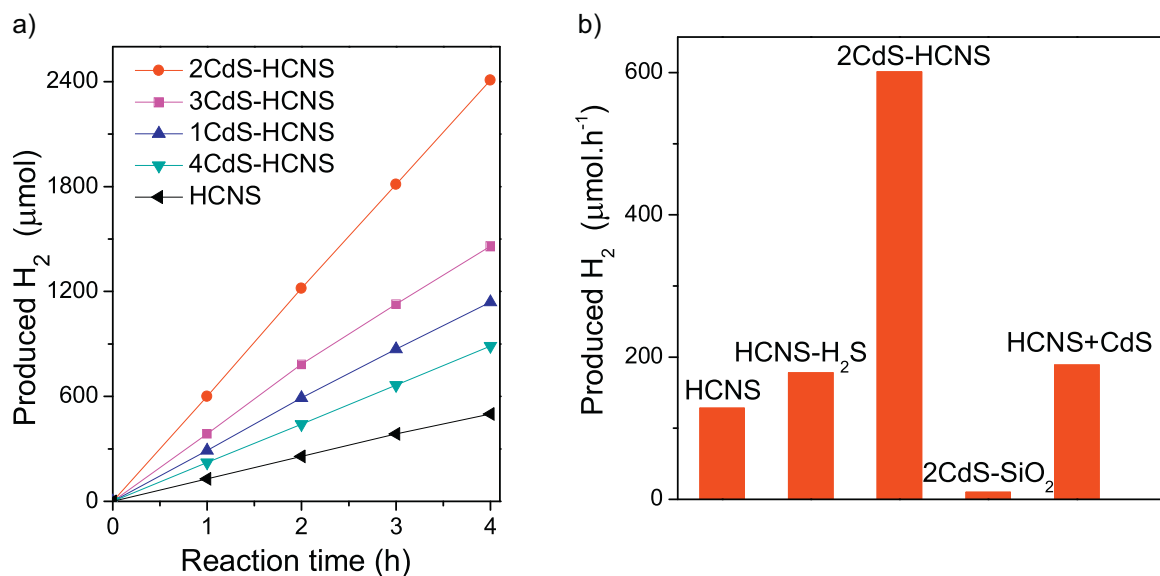


Fig. 8. Photocatalytic hydrogen evolution by CdS-HCNS photocatalysts under visible light irradiation ($\lambda > 420 \text{ nm}$), (a) with different amounts of CdS QDs; (b) with some reference samples of HCNS, HCNS- H_2S , 2CdS- SiO_2 , physically-mixed HCNS and CdS.

as confirmed by the solid state ^{13}C NMR analysis (Fig. S1) [39–40]. These results suggest that the chemical structure of HCNS is mostly unaltered after the modification of a small amount of CdS QDs that is enough to modify the semiconductive properties.

The optical and electrochemical properties of $x\text{CdS-HCNS}$ were characterized by means of UV-visible absorption spectra, photoluminescence (PL) emission spectrum, electron paramagnetic resonance (EPR) spectra, and electrochemical impedance spectroscopy (EIS). Our results of optical absorption measurements demonstrate that all $x\text{CdS-HCNS}$ samples show strong absorption capability in the optical region from ultraviolet to 520 nm as shown in Fig. 6a. We interpret this to the fierce interaction between HCNS and CdS QDs. Note that the absorption peaks of pure CdS QDs at 520 nm are blue-shifted when compared to those of CdS (Fig. 6a insert), due to the quantization size effects of the ultrafine nanoparticles [19]. Furthermore, the absorbance at 520 nm increased with successive deposition of higher amounts of CdS QDs.

The charge-carriers separation/recombination rates of the photo-excited carriers were next investigated by room temperature PL under excitation wavelength of 400 nm, because they are key parameters in determining the photocatalytic performance. As shown in Fig. 6b, a strong PL emission peak is observed for the pristine HCNS, which is attributed to the radiative recombination of charge carriers. This recombination process can be greatly suppressed by introducing CdS QDs on HCNS surface. This should be attributed to the heterostructure system that indeed promotes the separation and migration of photogenerated charges, with the localization of electrons in one side (CdS QDs) and holes in the other side (HCNS) by the band offsets. The lower recombination rate of charge carriers is proposed to facilitate photocatalysis. Insight into the charge separation in the sample is further revealed by the room-temperature electron paramagnetic resonance (EPR) (Fig. S2) and the following (photo) electrochemical characterizations.

The pure HCNS and $x\text{CdS-HCNS}$ samples were evaluated by the photo-electrochemical experiments. EIS study of the charge transfer rate in the dark reveals the expected semicircular Nyquist plots for HCNS and 2CdS-HCNS. A significantly decreased semidiameter for 2CdS-HCNS (Fig. 7a) is observed, suggesting an efficient separation of electron-hole pairs and a fast interfacial charge transfer occurring on the CdS-HCNS. The transient photocurrent responses of $x\text{CdS-HCNS}$ and pure HCNS samples were investigated for sev-

eral on-off cycles of irradiation. As shown in Fig. 7b, an enhanced photocurrent for 2CdS-HCNS is generated, which is nearly 3 times higher than that of the pure HCNS, strongly illustrating that the mobility of the charge carriers is promoted. This result suggests that the improved efficiency of charge separation and the prolonged lifetime of charge carriers are realized in the CdS-HCNS system [41–42]. Thus, the drawbacks of fast charge recombination in HCNS photocatalysts have been addressed by the construction of heterostructures, and a better photocatalytic performance can be expected.

The photocatalytic activities of the heterostructural samples were evaluated in an assay of visible-light-induced H_2 production. As shown in Fig. 8a, all heterojunctions demonstrate an enhanced H_2 evolution rate (HER) in comparison with the pristine HCNS. The optimum HER of $601 \mu\text{mol h}^{-1}$ is achieved for 2CdS-HCNS, which is about 5 times faster than that of the pure one. To better understand this, pure HCNS, 2CdS- SiO_2 , as well as HCNS- H_2S were selected as the references and tested under the experimental conditions similar to CdS-HCNS (Fig. 8b). The HER of HCNS- H_2S is determined as $178 \mu\text{mol h}^{-1}$, slightly higher than pure HCNS ($128 \mu\text{mol h}^{-1}$), but far less than all $x\text{CdS-HCNS}$ samples. The HER of 2CdS- SiO_2 is tested as $10 \mu\text{mol h}^{-1}$, far less than $601 \mu\text{mol h}^{-1}$. These results are confirmed that the high photocatalytic performance was promoted by the generation of iso-type heterostructures, rather than the change of physical/chemical characters induced by post-modification treatment. To further underline the necessity of intimate contact between the host and the guest materials, HCNS and CdS QDs (4 mg) were just physically mixed for photocatalytic H_2 evolution test under the same reaction conditions. As expected, there is no significant enhancement could be found. These above results reveal that heterojunctions system of HCNS and CdS QDs indeed remarkably improves the photocatalytic efficiency.

It is generally accepted that photocatalytic activity is mainly governed by light-absorption ability, surface properties (including adsorption property, specific surface area, etc.), and photogenerated charge-separation efficiency. The CdS QDs depositing indeed substantially influenced the light absorption property and specific surface area of HCNS. However, these low hydrogen-production rate by HCNS+CdS ($189 \mu\text{mol h}^{-1}$) and HCNS- H_2S ($178 \mu\text{mol h}^{-1}$) samples, indicating that these two factors are not crucial to the

photocatalytic activity for CdS-HCNS composites. The origin of the enhanced photocatalytic activity was attributed to the formation of surface heterostructure between CdS QDs and HCNS, by accelerating the separation and migration rate of charge carriers. The schematic representation of the photogenerated charge-transfer process in CdS-HCNS composites is illustrated in Fig. 9. Basically, when the samples were illuminated with visible light, electrons and holes can be effectively excited in HCNS and CdS QDs. As the conduction band of the HCNS is more negative than that of the CdS QDs, an internal local electric field is therefore generated. This makes the electrons quickly transfer to the conduction band of CdS QDs, then, the excited electrons will accumulate on the Pt nanoparticles and then participate in H_2 evolution. For the CdS QDs, the photogenerated holes can rapidly migrate to the HCNS and the photocorrosion of CdS QDs is substantially alleviated [43–44]. However, when the amounts of CdS QDs go beyond 30 wt.%, evidently decreased HER was received. This is mainly due to the excessive deposition of CdS particles that virtually cause a serious particle accumulation (Fig. 10).

Wavelength-dependent H_2 production experiments show that the H_2 evolution activity of 2CdS-HCNS is well consistent with its optical absorption curve (Fig. 11a). This supports that the main driving force of the photocatalytic reaction is the harvested photons that excite electrons and holes in the composite semiconductor to induce surface redox reactions. Meanwhile, when extending the wavelength of incident light to 550 nm, the 2CdS-HCNS sample still

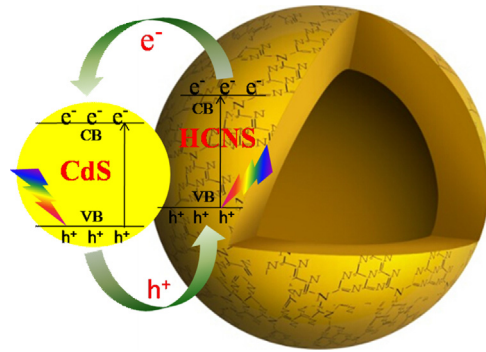


Fig. 9. Schematic illustration of CdS-HCNS heterojunction system.

shows much enhanced photocatalytic activity ($HER = 70 \mu\text{mol h}^{-1}$), while the pure HCNS is practically inert (with HER less than $1 \mu\text{mol h}^{-1}$). The stability of the optimized 2CdS-HCNS sample in a long time course hydrogen evolution reaction under illumination of visible spectrum ($\lambda > 420 \text{ nm}$) is also investigated. The evolved H_2 gases increase steadily as a function of irradiation time, as showed in Fig. 11b. After a continuous reaction for 4 h, the gathered gases reached about 2.4 mmol. Moreover, after six repeat reaction cycles, no noticeable deactivation in the hydrogen evolution can be obtained. The solution of after photocatalytic reaction has been

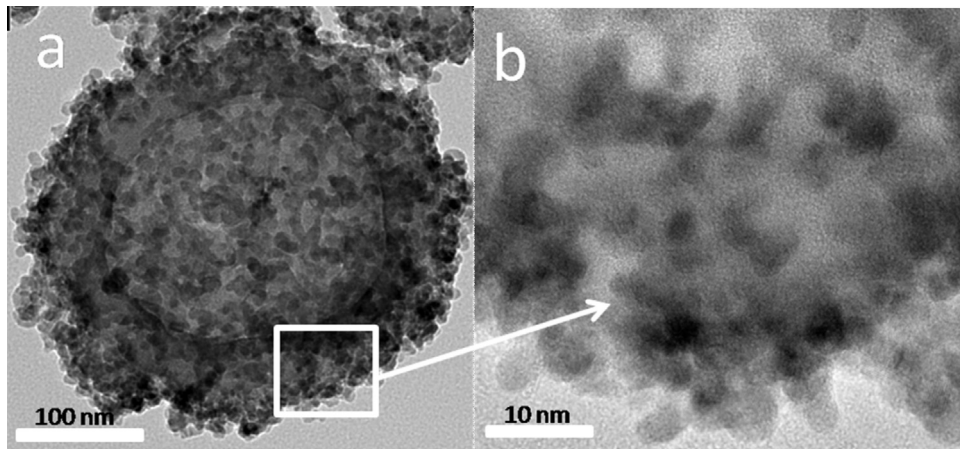


Fig. 10. TEM images of 4CdS-HCNS sample with excess amounts of CdS QDs.

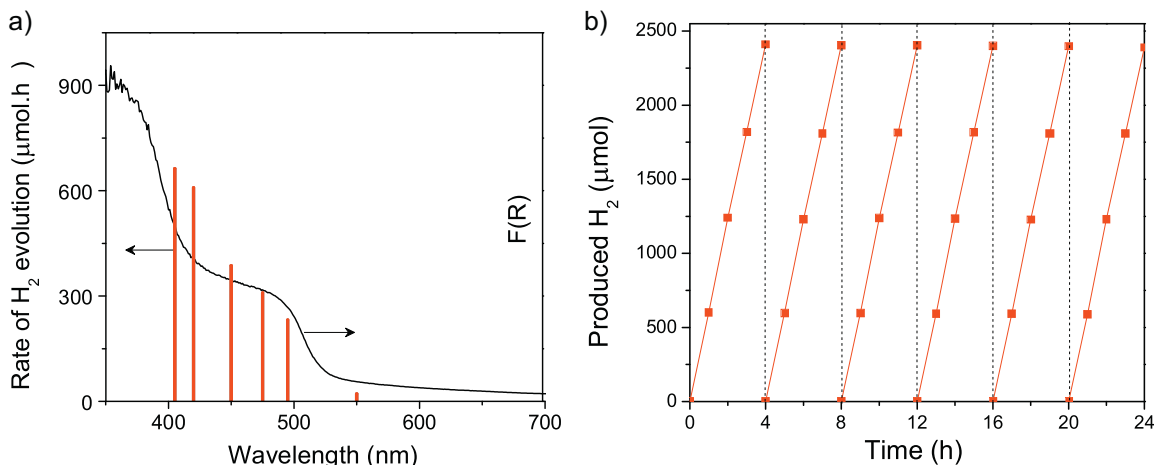


Fig. 11. (a) wavelength-dependent H_2 evolution rates under visible light using colored filters (long pass cut-off filters) and (b) the stability test of 2CdS-HCNS under visible light irradiation at $\lambda > 420 \text{ nm}$.

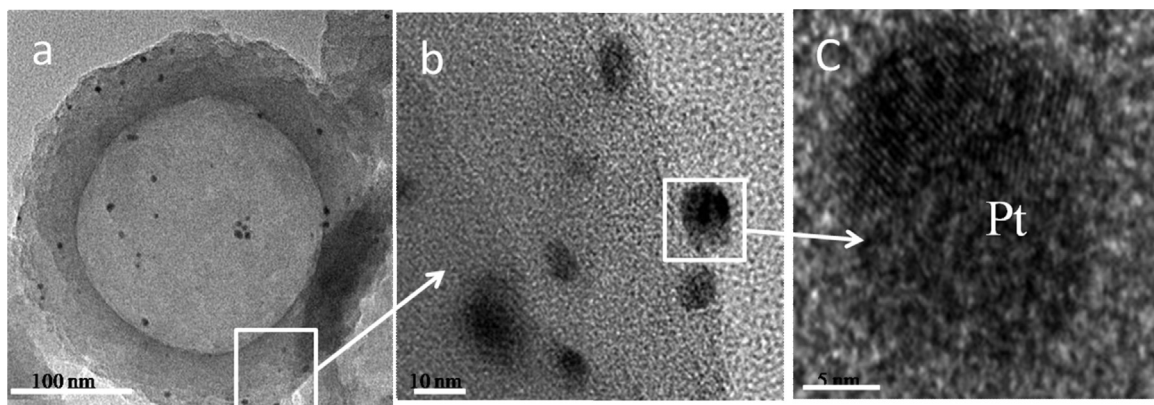


Fig. 12. TEM images of the Pt/2CdS-HCNS sample recovered after the photocatalytic reaction.

tested by inductively coupled plasma mass spectrometry (ICP-MS). The concentration of released Cd²⁺ is only about 7.24×10^{-3} mg/L after 24 h photocatalytic reaction, much lower than the theoretical concentration of Cd in the reaction solution (40 mg/L). These results indicate that the well-developed heterojunctions could efficiently suppress the self-photocorrosion of CdS due to the inter-particle charge separation.

The well retained physicochemical properties in both structures and morphologies could be further certified by TEM, XRD, FT-IR, XPS, and PL analysis of the recycled catalysts. As displayed in Fig. 12, TEM observation indicates that the morphology and structure of the CdS-HCNS composites were essentially unchanged after the reaction. The XRD and FT-IR patterns (Fig. 13a–b) indicate that there is no remarkable alteration in the structure of the photocat-

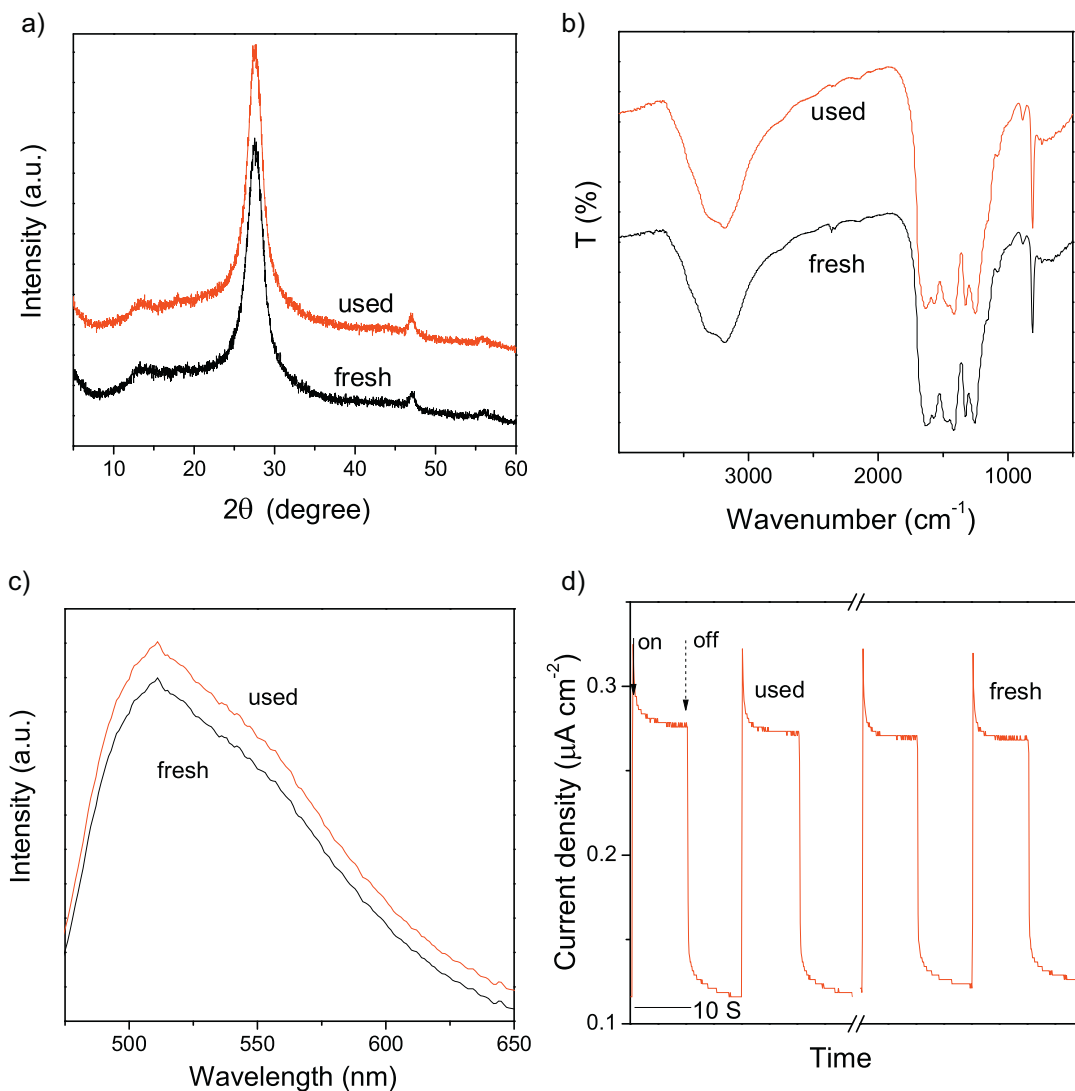


Fig. 13. Structure of 2CdS-HCNS before and after the photochemical reaction. (a) XRD pattern, (b) FTIR spectra, (c) PL spectra, and (d) photocurrent generation performance.

alyst before and after photoreaction, which was also proved by the XPS spectra (Fig. S3). The BE of C1s, N1s, S2p and Cd3d before and after photoreaction were nearly the same, suggesting that chemical states of S2p and Cd3d element of CdS-HCNS composites remained unchanged. These observations all support the robust nature and high operation stability of the inorganic-polymeric junctions for photocatalyzing hydrogen evolution. After that, the sample after the reaction was investigated by PL. As shown in Fig. 13c, the sample before and after reaction both exhibit the nearly identical PL emissions, implying that there are no remarkable changes for the electronic structure and surface active sites of CdS-HCNS after and before reaction, as also confirmed by photoelectrochemical measurements (Fig. 13d).

4. Conclusion

In summary, hybrid nanoarchitectures based on the deposition of CdS QDs onto HCNS exterior surfaces provide a valuable platform for constructing photosynthetic systems for hydrogen synthesis with visible light. The CdS-HCNS heterostructure exhibits a high stability under light irradiation. The enhanced photocatalytic activity and desirable photostability is attributed to the unique 3D hollow soft architectures of HCNS that can provide an intimate and flexible interfacial contact with QDs to create space charge accumulation/depletion junctions that promote the separation of photoinduced electrons and holes. This work unravels the potential of the developed CdS-HCNS nanohybrids in sustainable hydrogen production. We also anticipate that it will provide new opportunities for the innovative design and development of functional composites and devices based on the surface control on the physics and chemistry of the hollow conjugated polymers by modification with optic, magnetic and electronic cofactors to produce unique functions and properties.

Acknowledgements

This work was financially supported by the National Basic Research Program of China (2013CB632405), the National Natural Science Foundation of China (21425309 and 21173043), the State Key Laboratory of NBC Protection for Civilian (SKLNBC2013-04K), and the Specialized Research Fund for the Doctoral Program of Higher Education (20133514110003).

Appendix A. Supplementary data

Supplementary data associated with this article can be found, in the online version, at <http://dx.doi.org/10.1016/j.apcatb.2015.05.060>.

References

- [1] S. Hu, M. Shaner, J. Beardslee, M. Lichterman, B. Brunschwig, N. Lewis, *Science* 344 (2014) 1005–1009.
- [2] Y. Yin, R. Rioux, C. Erdonmez, S. Hughes, G. Somorjai, A. Alivisatos, *Science* 304 (2004) 711–714.
- [3] T. Ma, S. Dai, M. Jaroniec, S. Qiao, *Angew. Chem. Int. Ed.* 53 (2014) 7281–7285.
- [4] G. Zhang, H. Wu, T. Song, U. Paik, X. Lou, *Angew. Chem. Int. Ed.* 53 (2014) 12590–12593.
- [5] Y. Xia, X. Xia, Y. Wang, S. Xie, *MRS Bull.* 38 (2013) 335–343.
- [6] X. Peng, L. Manna, W. Yang, J. Wickham, E. Scher, A. Kadavanich, A. Alivisatos, *Nature* 404 (2000) 59–61.
- [7] N. Dasgupta, J. Sun, S. Britzman, J. Andrews, H. Lim, R. Gao, P. Yan, Yang, *Adv. Mater.* 26 (2014) 2137–2184.
- [8] Y. Xie, Z. Yu, G. Liu, X. Ma, H. Cheng, *Energy Environ. Sci.* 7 (2014) 1895–1901.
- [9] H. Tada, T. Mitsui, T. Kiyonaga, T. Akita, K. Tanaka, *Nat. Mater.* 5 (2006) 782–786.
- [10] K. Maeda, D. Lu, K. Domen, *Angew. Chem. Int. Ed.* 52 (2013) 6488–6491.
- [11] P. Zhou, J. Yu, M. Jaroniec, *Adv. Mater.* 26 (2014) 4920–4935.
- [12] K. Liu, R. Xing, C. Chen, G. Shen, L. Yan, Q. Zou, G. Ma, H. Möhwald, X. Yan, *Angew. Chem. Int. Ed.* 54 (2015) 500–505.
- [13] J. Kim, M. Lee, J. Lee, C. Park, *Angew. Chem. Int. Ed.* 51 (2012) 517–520.
- [14] Q. Zou, L. Zhang, X. Yan, A. Wang, G. Ma, J. Li, H. Möhwald, S. Mann, *Angew. Chem. Int. Ed.* 54 (2014) 2366–2370.
- [15] J. Zhang, Z. Zhu, Y. Tang, K. Müllen, X. Feng, *Adv. Mater.* 26 (2014) 734–738.
- [16] Q. Li, B. Guo, J. Yu, J. Ran, B. Zhang, H. Yan, J. Gong, *J. Am. Chem. Soc.* 133 (2011) 10878–10884.
- [17] Y. Hu, X. Gao, L. Yu, Y. Wang, J. Ning, S. Xu, X. Lou, *Angew. Chem. Int. Ed.* 52 (2013) 5636–5639.
- [18] C. Eley, T. Li, F. Liao, S. Fairclough, J. Smith, G. Smith, S. Tsang, *Angew. Chem. Int. Ed.* 53 (2014) 7838–7842.
- [19] D. Baker, P. Kamat, *Adv. Funct. Mater.* 19 (2009) 805–811.
- [20] J. Chen, X. Wu, L. Yin, B. Li, X. Hong, Z. Fan, B. Chen, C. Xue, H. Zhang, *Angew. Chem. Int. Ed.* 54 (2014) 1210–1214.
- [21] H. Bao, Y. Gong, Z. Li, M. Gao, *Chem. Mater.* 16 (2004) 3853–3859.
- [22] X.C. Wang, K. Maeda, A. Thomas, K. Takanabe, G. Xin, J. Carlsson, K. Domen, M. Antonietti, *Nat. Mater.* 8 (2009) 76–80.
- [23] C. Caputo, M. Gross, V. Lau, C. Cavazza, B. Lotsch, E. Reisner, *Angew. Chem. Int. Ed.* 53 (2014) 11538–11542.
- [24] J.S. Zhang, M.W. Zhang, L.H. Lin, X.C. Wang, *Angew. Chem. Int. Ed.* 54 (2015) 6297–6301.
- [25] J. Fu, B. Chang, Y. Tian, F. Xi, X. Dong, *J. Mater. Chem. A* 1 (2013) 3083–3090.
- [26] S. Cao, Y. Yuan, J. Fang, M. Shahjamali, F. Boey, J. Barber, S. Loo, C. Xue, *Int. J. Hydrogen Energy* 38 (2013) 1258–1266.
- [27] L. Ge, F. Zuo, J. Liu, Q. Ma, C. Wang, D. Sun, L. Bartels, P. Feng, *J. Phys. Chem. C.* 116 (2012) 13708–13714.
- [28] J. Zhang, Y. Wang, J. Jin, J. Zhang, Z. Lin, F. Huang, J. Yu, *Appl. Mater. Interfaces* 5 (2012) 10317–10324.
- [29] D. Zheng, C. Huang, X. Wang, *Nanoscale* 7 (2015) 465–470.
- [30] J.H. Sun, J.S. Zhang, M.W. Zhang, M. Antonietti, X.Z. Fu, X.C. Wang, *Nat. Commun.* 3 (2012) 1139–1145.
- [31] J.S. Zhang, M.W. Zhang, C. Yang, X.C. Wang, *Adv. Mater.* 26 (2014) 4121–4126.
- [32] Y. Jun, J. Park, S. Lee, A. Thomas, W. Hong, G. Stucky, *Angew. Chem. Int. Ed.* 52 (2013) 11083–11087.
- [33] M. Bhunia, K. Yamauchi, K. Takanabe, *Angew. Chem. Int. Ed.* 53 (2014) 11001–11005.
- [34] J. Liu, J. Wang, Z. Wang, W. Huang, S. Yu, *Angew. Chem. Int. Ed.* 53 (2014) 133477–133482.
- [35] Y. Zhang, Q. Pan, G. Chai, M. Liang, G. Dong, Q. Zhang, J. Qiu, *Sci. Rep.* 3 (2013) 1943–1950.
- [36] P. Niu, L. Zhang, G. Liu, H. Cheng, *Adv. Funct. Mater.* 22 (2012) 4763–4770.
- [37] G. Siller, N. Severin, S. Chong, T. Björkman, R. Palgrave, A. Laybourn, M. Antonietti, Y. Khimyak, A. Krasheninnikov, J. Rabe, U. Kaiser, A. Cooper, A. Thomas, M. Bojdys, *Angew. Chem. Int. Ed.* 53 (2014) 7450–7455.
- [38] Y. Zheng, L.H. Lin, X.J. Ye, F.S. Guo, X.C. Wang, *Angew. Chem. Int. Ed.* 53 (2014) 11926–11930.
- [39] D. Martin, K. Qiu, S. Shevlin, A. Handoko, X. Chen, Z. Guo, J. Tang, *Angew. Chem. Int. Ed.* 53 (2014) 9240–9245.
- [40] G. Zhang, M. Zhang, X. Ye, X. Qiu, S. Lin, X. Wang, *Adv. Mater.* 26 (2014) 805–809.
- [41] Y. Zheng, Y. Jiao, J. Chen, J. Liu, J. Liang, A. Du, W. Zhang, Z. Zhu, S. Smith, M. Jaroniec, Gao, Lu, S. Qiao, *J. Am. Chem. Soc.* 133 (2015) 20116–20119.
- [42] M.W. Zhang, X.C. Wang, *Energy Environ. Sci.* 7 (2014) 1902–1906.
- [43] M. Shalom, S. Gimenez, F. Schipper, I. Cardona, J. Bisquert, M. Antonietti, *Angew. Chem. Int. Ed.* 53 (2014) 3654–3658.
- [44] J.S. Zhang, M.W. Zhang, R.Q. Sun, X.C. Wang, *Angew. Chem. Int. Ed.* 51 (2012) 10145–10149.